ADVANCED QUANTUM TECHNOLOGIES
www.advquantumtech.com

Topological Properties of a Non-Hermitian Quasi-1D Chain with a Flat Band

C. Martínez-Strasser, M. A. J. Herrera, A. García-Etxarri, G. Palumbo, F. K. Kunst, and D. Bercioux**

The spectral properties of a non-Hermitian quasi-1D lattice in two of the possible dimerization configurations are investigated. Specifically, it focuses on a non-Hermitian diamond chain that presents a zero-energy flat band. The flat band originates from wave interference and results in eigenstates with a finite contribution only on two sites of the unit cell. To achieve the non-Hermitian characteristics, the system under study presents non-reciprocal hopping terms in the chain. This leads to the accumulation of eigenstates on the boundary of the system, known as the non-Hermitian skin effect. Despite this accumulation of eigenstates, for one of the two considered configurations, it is possible to characterize the presence of non-trivial edge states at zero energy by a real-space topological invariant known as the biorthogonal polarization. This work shows that this invariant, evaluated using the destructive interference method, characterizes the non-trivial phase of the non-Hermitian diamond chain. For the second non-Hermitian configuration, there is a finite quantum metric associated with the flat band. Additionally, the system presents the skin effect despite the system having a purely real or imaginary spectrum. The two non-Hermitian diamond chains can be mapped into two models of the Su-Schrieffer-Heeger chains, either non-Hermitian, and Hermitian, both in the presence of a flat band. This mapping allows to draw valuable insights into the behavior and properties of these systems.

1. Introduction

Non-Hermitian (NH) physics is an emergent field of research that has important implications both for quantum and classical physics.[1–6] A systematic study of this field started with the cornerstone works by Bender and Boettcher on Hamiltonian systems preserving the combination of parity and time-reversal ($\mathcal{PT}$) symmetry, ensuring a real spectrum.[7,8] At the moment, model Hamiltonian systems respecting $\mathcal{PT}$ symmetry are considered excellent models for describing dissipative systems with balanced gain and loss in an effective way.[1]

The condition of reality of the spectrum can be extended by considering a more general symmetry class known as *pseudo-Hermiticity* that includes the $\mathcal{PT}$-one.[9] In general, NH operators exhibit intriguing phenomena such as non-orthogonal eigenstates and complex energy spectra containing exceptional points (EPs), representing stable points of band degeneracies at which not only the eigenvalues but also the eigenvectors coalesce.[1,3,4]

Recent research has focused on the topological characterization of NH systems,[1,3,4] expanding upon the framework established for Hermitian condensed-matter systems. One of the key effects of moving to the NH realm leads to the extension of the topological classification, considering now that complex conjugation and transposition are no longer equivalent for non-Hermitian Hamiltonians, moving to 38 classes[10] instead of the tenfold classification of the Hermitian counterpart.[11]

A key difference between NH and Hermitian systems is the breakdown of the traditional bulk-boundary correspondence

C. Martínez-Strasser, M. A. J. Herrera
Department of Physics
University of the Basque Country UPV/EHU
Apartado 644, 48080 Bilbao, Spain
E-mail: carolina.martinez@dipc.org

C. Martínez-Strasser, M. A. J. Herrera, A. García-Etxarri, D. Bercioux
Donostia International Physics Center (DIPC)
20018 Donostia–San Sebastián, Spain
E-mail: dario.bercioux@dipc.org

C. Martínez-Strasser, F. K. Kunst
Max Planck Institute for the Science of Light
Staudtstraße 2, 91058 Erlangen, Germany

A. García-Etxarri, D. Bercioux
IKERBASQUE
Basque Foundation for Science
Plaza Euskadi 5, 48009 Bilbao, Spain

G. Palumbo
School of Theoretical Physics
Dublin Institute for Advanced Studies
10 Burlington Road, Dublin D04 C932, Ireland

The ORCID identification number(s) for the author(s) of this article can be found under https://doi.org/10.1002/qute.202300225

DOI: 10.1002/qute.202300225

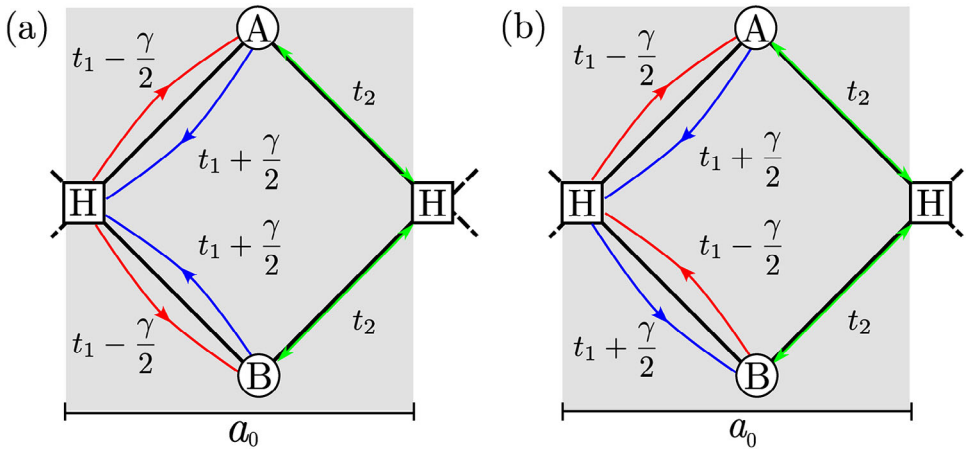

Figure 1. Sketch of the non-Hermitian diamond lattice in the A and B configurations, panel (a) and (b), respectively. The gray area denotes the unit cell of each lattice configuration. The lattice periodicity is a_0. In both panels, the blue arrows correspond to a hopping term of strength $t_1 + \frac{\gamma}{2}$, whereas the red ones to $t_1 - \frac{\gamma}{2}$.

(BBC), which predicts the appearance of boundary modes based on bulk topological invariants. This breakdown can be manifested through the non-Hermitian skin effect, where bulk states accumulate at the edges of the system.[12–14] Two possible research lines have been developed for reestablishing the BBC. The first one is based on the biorthogonal bulk-boundary correspondence approach[15]; here, right and left eigenvectors of the system under open boundary conditions (OBCs) are combined to project the boundary mode localization and predict gap closings accurately. The second method is based on the concept of the so-called *generalized Brillouin zone* (BZ),[12,16,17] in which additional information is encoded inside the standard Bloch bands.

For the investigation of topological effects in NH systems, 1D systems are ideal platforms for presenting the key features.[15,18–21] These simple 1D models exhibit many of the unusual properties of NH systems. A paradigmatic example is the Hatano-Nelson model,[18] which is a one-band system with anisotropic nearest-neighbor couplings originally proposed to study localization transitions in superconductors. Under periodic boundary conditions (PBCs), this model features loops in the complex spectrum resulting in a non-trivial spectral winding number.[22,23] When going to OBCs, this translates into the appearance of the NH skin effect, thus establishing a new, truly NH bulk-boundary correspondence.[24–26]

Even richer NH phenomena can be observed in NH versions of the Su-Schrieffer-Heeger (SSH) chains.[27–29] This 1D two-band system features zero-energy end modes in the Hermitian case, which are topologically protected by a non-trivial winding number. A NH version of this chain with asymmetric hopping has been shown to host zero-energy boundary states as well as NH skin states.[12,15] As such, this system breaks the conventional BBC and needs to be treated either in the biorthogonal picture[15] or within the framework of the generalized BZ.[12] A $\mathcal{PT}$-symmetric version of the SSH chain has also been studied, which features an onsite complex potential with alternating sign.[20,30] In this case, the boundary states acquire an imaginary energy, while the NH skin effect is absent, such that the traditional BBC applies.

In this work, we present the topological properties of a quasi-1D system: the diamond chain (DC).[31–34] The unit cell of this quasi-1D system contains three sites with unequal connectivity; in the following, we will name the site with higher connectivity as H, whereas the sites with lower connectivity will be named A and B| see **Figure 1**. This lattice model has also been studied with respect to the effects of localization due to an external magnetic field and many-body effects.[31,35,36] The imbalance in the connectivity results in the appearance of a bulk zero-energy mode, where the wave function is localized only in the sites of lower connectivity with opposite amplitudes, while it has zero amplitude on the remaining H sites. In the Hermitian case, in Ref. [34], it was shown that two possible dimerizations could be chosen for the DC, but only one of these presents topological properties analogous to the SSH model.[27–29] Possible experimental implementations for the Hermitian system involve cold atoms in optical lattices,[37] photonic,[38] and solid-state platform.[39] Within this work, we investigate two possible NH configurations of the DC chain. A NH version of the DC has already been investigated with particular emphasis on possible photonic realizations and focusing mainly on the $\mathcal{PT}$-symmetric version.[3,40–45] Additional research has investigated the possibility of obtaining lasing from the flat band.[46] Within this work, we will relax this symmetry constriction.

We introduce non-Hermiticity by imposing a preferred hopping direction within unit cells, resulting in two non-reciprocal tight-binding models. The motivation beyond studying the NH diamond lattice stems from its potential for realizing two distinct dimerization configurations within the lattice. The first configuration displays zero-energy edge states, which can be characterized through the evaluation of the biorthogonal polarization.[15,21] The interest in the second configuration arises from the properties of the flat band[47–49] resulting in a *giant boost* of the quantum metric properties.[50] Additionally, we show how to map these two systems into a combination of Hermitian and NH SSH models coupled to a flat band. This mapping allows us to draw valuable insights into the behavior and properties of these systems, opening new avenues for further exploration of non-Hermitian 1D systems.

This article is structured as follows: in Section 2, we describe the NH DC in the two possible dimerization configurations that we have uncovered. In Section 3, we explore the topological properties of these two NH lattice configurations, focusing in particular on the biorthogonal polarization and the quantum metric. In Section 4, we present the path toward the unitary transformation of the lattices into SSH chains, plus an extra site describing the flat band. We conclude in Section 5 with a summary of our findings. We include technical appendices: Appendix A.1 presenting an analytical expression for the system wave functions in the case of translational invariance, and Appendix A.2 summarizing the symmetry properties is the two lattices at the end of our work.

2. Results

2.1. Systems and Formalisms

2.1.1. Spectrum and Symmetries

The non-Hermitian counterpart of the diamond chain under "lattice I" configuration from Ref. [34] can be divided into two different systems according to their NH coupling configuration — DCA and DCB. The main differences imply an intracell hopping from site H to site B of $t_1 - \gamma/2$ in DCA and $t_1 + \gamma/2$ in DCB. We present a sketch of these two lattices in Figure 1. In the NH version, both lattice systems still present a zero-energy flat band in the energy spectrum; this originates in the unequal connectivity between the three lattice sites in the unit cell| H connected to four neighbors, and A and B connected to two. The two chains could be thought of as two joined NH SSH models[20]; however, the sharing of a common lattice site (H) drastically changes the spectral properties of both the Hermitian and NH systems.

2.1.2. Diamond Chain A (DCA)

The tight-binding Hamiltonian of the non-Hermitian diamond chain in the DCA configuration [see Figure 1a)] reads:

$$\begin{aligned}\mathcal{H}_{\mathrm{DCA}} = \sum_n \Big\{ &\Big[t_2(c^\dagger_{\mathrm{A},n} + c^\dagger_{\mathrm{B},n})c_{\mathrm{H},n+1} + \mathrm{h.c.}\Big] \\ &+\Big(t_1 - \frac{\gamma}{2}\Big)(c^\dagger_{\mathrm{A},n} + c^\dagger_{\mathrm{B},n})c_{\mathrm{H},n} \\ &+\Big(t_1 + \frac{\gamma}{2}\Big)c^\dagger_{\mathrm{H},n}(c_{\mathrm{A},n} + c_{\mathrm{B},n})\Big\}\end{aligned} \tag{1}$$

The operators $c^\dagger_{\alpha,n}$ and $c_{\alpha,n}$ create and annihilate a state on sub-lattice site $\alpha \in \{\mathrm{A}, \mathrm{B}, \mathrm{H}\}$ of unit cell n, respectively. Here, n ranges from 1 to N, where N is the total number of unit cells. The parameters t_1 and t_2 represent the intracell and intercell hopping parameters, respectively, while γ is an asymmetry term that introduces the non-Hermitian character into the system| see Figure 1a. Throughout this paper, we fix all these parameters to be real-valued, i.e., $\{t_1, t_2, \gamma\} \in \mathbb{R}$.

Assuming translational invariance, the NH Hamiltonian operator can be written in reciprocal space as

$$h_{\mathrm{DCA}}(\kappa) = d_x\Sigma_x + d_y\Sigma_y \tag{2}$$

after an overall rotation $e^{i\kappa/2}$ over H sites in reciprocal space, where $\kappa = ka_0$ is a real and dimensionless quasi momentum, a_0 is the lattice periodicity constant, and the momentum $k \in \mathrm{BZ}$. We have defined the matrices Σ_x and Σ_y as:

$$\Sigma_x = \frac{1}{\sqrt{2}}\begin{pmatrix}0&1&0\\1&0&1\\0&1&0\end{pmatrix} \text{ and } \Sigma_y = \frac{1}{\sqrt{2}}\begin{pmatrix}0&\mathrm{i}&0\\-\mathrm{i}&0&-\mathrm{i}\\0&\mathrm{i}&0\end{pmatrix} \tag{3a}$$

accompanied by

$$\Sigma_z = \frac{1}{2}\begin{pmatrix}1&0&1\\0&-2&0\\1&0&1\end{pmatrix} \text{ and } \tilde{\mathbb{I}} = \frac{1}{2}\begin{pmatrix}1&0&1\\0&2&0\\1&0&1\end{pmatrix} \tag{3b}$$

Therefore, the characteristic $\boldsymbol{d}$-vector, $\boldsymbol{d} = (d_x, d_y, d_z)$ reads explicitly

$$\boldsymbol{d}(\kappa) = \sqrt{2}(t_1 + t_2\cos(\kappa), t_2\sin(\kappa) + \mathrm{i}\gamma/2, 0) \tag{4}$$

It has to be noted that the set $\{\tilde{\mathbb{I}}, \Sigma_x, \Sigma_y, \Sigma_z\}$ forms an orthogonal base with SU(2) Lie algebra with $[\Sigma_n, \Sigma_m] = 2i\epsilon_{nmk}\Sigma_k\tilde{\mathbb{I}}$ and $\{\Sigma_n, \Sigma_m\} = 2\delta_{nm}\tilde{\mathbb{I}}$, where ϵ_{nmk} is the Levi-Civita tensor with $n, m, k \in \{x, y, z\}$, and $[.,.]$ and $\{.,.\}$ are the commutator and the anticommutator, respectively.[34]

The representation in Equation (2) results in a three-band model. This can be considered equivalent to the one obtained for the NH SSH two-band model[15,51] with the inclusion of a zero-energy flat band. This analogy will be made more explicit in Section 4.

The energy spectrum of DCA is

$$E^{\mathrm{DCA}}_\alpha = \alpha\sqrt{2\left(t_1^2 + t_2^2\right) + 4t_1t_2\cos(\kappa) + 2\mathrm{i}\gamma t_2\sin(\kappa) - \frac{\gamma^2}{2}} \tag{5}$$

with $\alpha \in \{0, \pm\}$. We note in passing that this spectrum is identical to the NH-SSH model up to a factor $\sqrt{2}$,[15] see Equation (4). We present in Appendix A.1 the analytical expression of the eigenstates of Equation (2).

By inspecting the Jordan decomposition of the DCA Hamiltonian and the spectrum in Equation (5), we find four exceptional points at $\mathrm{Im}[E_\pm] = \mathrm{Re}[E_\pm] = 0$. These points are located at $t_1 = -t_2 \pm \gamma/2$ for $\kappa = 0$ and $t_1 = t_2 \pm \gamma/2$ for $\kappa = \pi$, recognizing the similarity with the standard non-Hermitian SSH model.[15] As κ ranges from 0 to 2π, the system's energy spectrum on the complex energy plane is formed of two bands and a zero-energy point that signals the zero-energy flat band of the system under OBC (see the inset of Figure 3). Depending on the choice of parameters, the two-band energies can either braid into two separate loops (inside which a reference point can be placed acting as a point gap) or into a single loop (also presenting a point gap).[48] Both phases display a qualitative change in the spectrum, in which the phase transitions correspond to the crossings of exceptional points at which the Hamiltonian becomes defective. We find a real and a fully imaginary gap for $\kappa = \{0, \pi\}$ with $|\gamma/2| \leq |t_1 \pm t_2|$ and $|\gamma/2| \geq |t_1 \pm t_2|$, respectively.

The finite-size system presents edge modes under the appropriate choice of system parameters. In **Figure 2**, we compare the energy spectrum|now denoted through $\mathcal{E}$| of a finite-size system

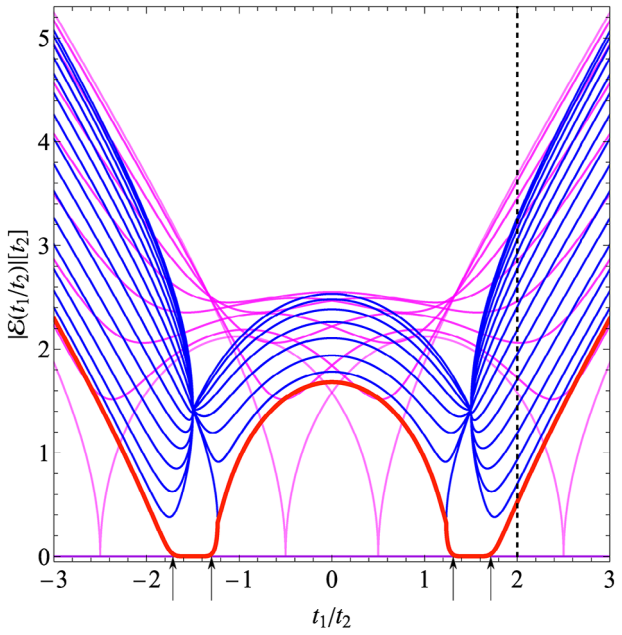

Figure 2. The absolute value of the eigenenergies is examined as a function of the hopping parameters, denoted as t_1, in the non-Hermitian DCA model with a fixed asymmetry term $\gamma = 3$ and a system size $N = 16$. The pink lines represent the bulk spectra obtained under periodic boundary conditions (PBC), and the blue (red) lines correspond to the bulk (edge) spectra obtained under open boundary conditions (OBC), signaling the phase-transition points through arrows.
The zero-energy flat band, depicted in purple, is present in both the PBC and OBC scenarios. Moreover, the black dashed line at $t_1/t_2 = 2$ indicates the hopping parameter values at which the skin effect in **Figure 3** has been computed.

with open boundary conditions, in which edge modes appear, and with periodic boundary conditions. In Section 3, we will characterize the presence of these edge states using the biorthogonal polarization,[15] enabling us to differentiate them from bulk eigenstates that pile up at the boundaries, a topologically trivial effect in non-Hermitian systems lacking parity symmetry. This is known as the non-Hermitian *skin* effect and corresponds to a piling of the system eigenstates at the system's boundary. We show

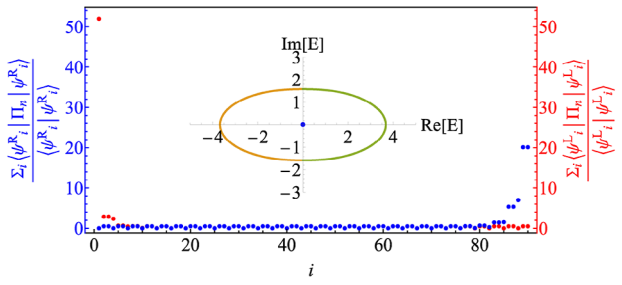

Figure 3. Skin effect of the non-Hermitian DCA chain represented through the sum of the squared amplitudes of each site i with $N = 30$, $\gamma = 3$ and $t_1/t_2 = 2$ To visualize the eigenstates, we are considering the base (H_n, A_n, B_n). Additionally, we are rescaling their expectation value for comparative reasons. Inset: complex plane with the corresponding positive(green), negative(yellow), and flat(blue) energy bands.

in Figure 3 the skin effect for left and right eigenstates for the DCA system. Upon evaluating the Jordan canonical form of the non-Hermitian DCA system at $t_1 = \gamma/2$, we find $N + 3$ independent eigenvectors, N corresponding to the zero-energy flat band and three corresponding to EPs. Similar to the non-Hermitian SSH.[52] From these three EPs, we obtain that two EPs are of higher order and are located at $\mathcal{E} = \pm\sqrt{2}t_2$, whereas the last one is a zero-energy EP of order two.

2.1.3. Diamond Chain B (DCB)

For the DCB lattice, the non-Hermitian tight-binding Hamiltonian will read:

$$\begin{aligned}\mathcal{H}_{\mathrm{DCB}} = \sum_n \Big\{ &\Big[t_2(c^\dagger_{\mathrm{A},n} + c^\dagger_{\mathrm{B},n})c_{\mathrm{H},n+1} + \mathrm{h.c.}\Big] \\ &+ \Big(t_1 + \frac{\gamma}{2}\Big)(c^\dagger_{\mathrm{H},n}c_{\mathrm{A},n} + c^\dagger_{\mathrm{B},n}c_{\mathrm{H},n}) \\ &+ \Big(t_1 - \frac{\gamma}{2}\Big)(c^\dagger_{\mathrm{A},n}c_{\mathrm{H},n} + c^\dagger_{\mathrm{H},n}c_{\mathrm{B},n})\Big\}\end{aligned} \tag{6}$$

in which the primary distinction compared to the DCA lattice is the orientation of the intracell hoppings ($t_1 \pm \gamma/2$) connecting the H and B sites| see Figure 1b. In the translational invariant form, the corresponding Hamiltonian cannot be expressed anymore only as a function of the characteristic vector **d** and the matrices in Equations (3), but requires the addition of the λ_7 Gell-Mann matrix:

$$h_{\mathrm{DCB}}(\kappa) = h_{\mathrm{DCA}}(\kappa) - \mathrm{i}\begin{pmatrix}0 & 0 & 0\\ 0 & 0 & -\mathrm{i}\\ 0 & \mathrm{i} & 0\end{pmatrix}\gamma \tag{7}$$

This last term is essential in order to change the sign of the non-reciprocal hopping term on the connections between the H and the B sites| see Figure 1b.

The corresponding energy spectrum reads

$$E^{\mathrm{DCB}}_\alpha = \alpha\sqrt{2\left(t_1^2 + t_2^2\right) + 4t_1t_2\cos(\kappa) - \frac{\gamma^2}{2}} \tag{8}$$

with $\alpha \in \{0, \pm\}$. Contrary to the case of DCA in Equation (5), here we no longer find terms coupling together γ with κ. We present in Appendix A.1 the analytical expression of the eigenstates of Equation (7).

Importantly, the expression for the energy spectrum for DCB is, up to a constant factor, the same as the energy spectrum for the $\mathcal{PT}$-symmetric NH-SSH model,[20] with the addition of a zero energy flat band. When the magnitudes of the first two terms in Equation (8) exceed that of the third term, a real gap emerges. Conversely, if the first two terms are smaller than the third term, an entirely imaginary gap is present. When plotted on the complex energy plane, contrary to the case of DCA, the eigenenergies (8) collapse into fully imaginary or real lines or a combination of both| see insets of Figure 5.

In spite of the similarities of the energy spectrum for a finite DCB system with a finite $\mathcal{PT}$-symmetric NH-SSH system (see **Figure 4**), the DCB model does not possess EPs under OBC due to

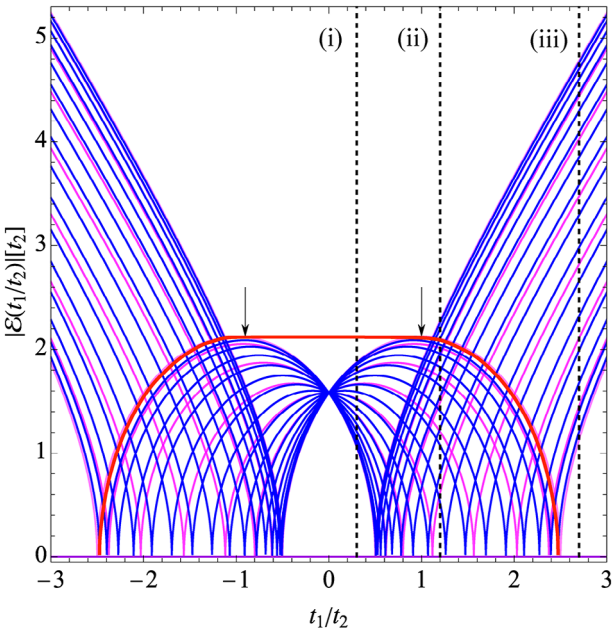

Figure 4. Absolute value of the eigenenergies as a function of the hopping parameters t_1 of the non-Hermitian DCB model for $\gamma = 3$ and $N = 16$. The pink lines depict the bulk spectra under periodic boundary conditions. The blue (red) lines correspond to the bulk (edge) spectra obtained under open boundary conditions (OBC), signaling the phase transition points through arrows. The black dashed lines indicate the specific values of the hopping parameters i) $t_1/t_2 = 0.3$, ii) $t_1/t_2 = 1.2$ and iii) $t_1/t_2 = 2.7$ at which the corresponding skin effects have been computed (see **Figure 5**). The zero-energy flat band is depicted in purple, present under both boundary conditions.

its non-Hermitian nature being attributed to non-reciprocal hoppings rather than on-site potentials. As a result, there is no phase transition between a $\mathcal{PT}$-broken and $\mathcal{PT}$-unbroken phase in the DCB model.The complex energy spectrum of the DCB collapsing into lines should signal the disappearance of the skin effect.[53] However, from Figure 5 ii,iii, we can clearly observe that the skin effect is still present for the DCB case despite the shape of the energy spectrum in the complex plane. We will give some additional insight into the skin effect of DCB in Section 3.

2.2. Topological Properties

In this section, we are going to explore the topological properties of DCA and DCB. While both exhibit edge modes, DCA possesses zero-energy edge modes, whereas DCB has them at finite energy. Additionally, the flat band eigenstate of the system for the DCB, unlike for DCA, is k-dependent| see Equations (A5a) and (A6a). Consequently, we will concentrate on characterizing non-trivial topological properties of the zero-energy modes on the DCA through the biorthogonal polarization.[1,15] Whereas, for the case of DCB, we will focus on the quantum metric properties of its flat band.

The DCA model exhibits several relevant symmetries considering the 38-fold classification typical on NH systems.[10] It presents the Hermitian conjugated particle-hole symmetry (PHS_c), with eigenenergies coming as either pure imaginary energies or pairs $(E(k), -E(-k)^*)$. Additionally, it shows the standard time-reversal symmetry (TRS_c), where eigenenergies come as real eigenvalues or in complex conjugate pairs, $(E(k), E(-k)^*)$. Moreover, the DCA model possesses the standard sublattice symmetry (SLS), for which the eigenvalues come in ± pairs at each k point. The DCB model shares the same symmetries as DCA and, in addition, possesses the Hermitian conjugated time-reversal symmetry (TRS_t) where the eigenenergies are paired by $(E(k), E(-k))$ and the standard pseudo-Hermiticity symmetry, which restricts the eigenenergies to be real. For a comprehensive overview of the symmetries discussed, please refer to the symmetry table in Appendix A.2.

2.2.1. Biorthogonal Polarization for DCA

In this section, we focus on the characterization of the zero-energy boundary modes of the non-Hermitian diamond chain and their localization over the parameter spectrum. We start by combining the left and right non-orthogonal eigenvectors of the non-Hermitian Hamiltonian operators to map the weight distribution of a given band—in this case, the edge-band—over the finite system.[54] This arrangement is obtained through the biorthogonal projection expectation value, $\langle \Pi_n \rangle_{\mathrm{LR}}$, also found as the biorthogonal density[15] where the biorthogonal projection operator is defined as $\Pi_n = \sum_\alpha |e_{\alpha,n}\rangle \langle e_{\alpha,n}|$ with $|e_{\alpha,n}\rangle = c^\dagger_{\alpha,n}|0\rangle$.[55] Therefore a real-parameter space topological invariant can be defined, namely the biorthogonal polarization:

$$\mathcal{P} = M - \lim_{N\to\infty} \langle \Psi_0^{\mathrm{L}} | N^{-1} \sum_{n=1}^{N} n \hat{\Pi}_n | \Psi_0^{\mathrm{R}} \rangle \tag{9}$$

where M is the number of boundary modes and $|\Psi_0^{\mathrm{R[L]}}\rangle$ are zero-energy right and left boundary modes. The biorthogonal polarization will therefore be $\mathcal{P} = M(0)$ when boundary states are present (absent) at the beginning of a quasi-1D chain. In order for the wave functions $|\Psi_0^{\mathrm{R[L]}}\rangle$ in Equation (9) to provide significant information for the appearance and the disappearance of boundary states in the corresponding lattices, the destructive interference method is used.

This local interference is naturally present on a quasi-1D lattice that begins and also ends with the same motif, in this case with an H site or with AB sites, under the constraint of presenting only nearest-neighbor hopping.[56,57] Under these circumstances, two chains can be obtained, the so-called broken chains, characterized by an exactly disappearing weight on one of the motifs. As a result, the localization factors of the broken chains' eigenmodes, $r_{\mathrm{L[R]}}$, can be exactly solved. These factors, whose magnitude will solely depend on the hopping terms $|r_{\mathrm{L[R]}}| = f(t_1, t_2, \gamma)$, will eventually give the dispersion rate of the eigenmode, signaling the parameter regions at which the topological phase transitions occur, i.e., at which the zero-energy wavefunctions correspond to bulk states $|r_{\mathrm{L}}^* r_{\mathrm{R}}| > 1$ or to boundary states $|r_{\mathrm{L}}^* r_{\mathrm{R}}| < 1$.[15] In spite of the eigenstates of the broken chains not being exact to the ones of the original unbroken chain, the phase transition points will stay unchanged up to finite-size effects in both broken and unbroken lattices.[15]

To further understand the destructive interference method, we will now solve the biorthogonal polarization for the DCA. The

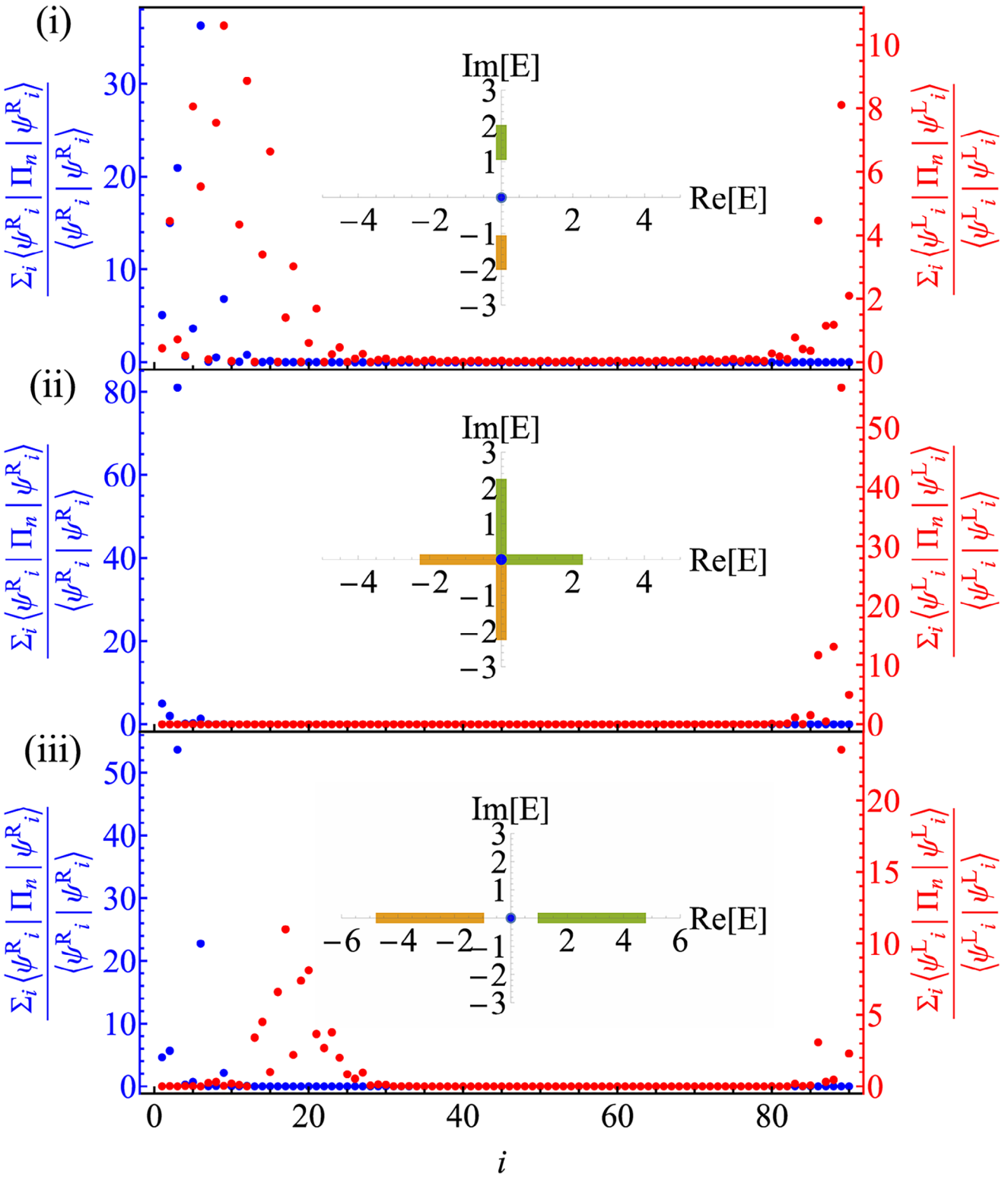

Figure 5. Skin effect of the non-Hermitian DCB chain represented through the sum of the squared amplitudes of each site i with $N = 30$ and $\gamma = 3$ considering the base (H_n, A_n, B_n). The upper diagram i) represents the sum of the squared amplitudes of each site considering the case in which the eigenvalues are fully imaginary pairs and where also edge states are present, like at $t_1/t_2 = 0.3$. The middle diagram ii) shows the skin effect under eigenvalues coming in complex conjugate pairs as in $t_1/t_2 = 1.2$, where the edge states are fading out into the bulk and the lower one iii) represents the case in which the spectra is fully real as it happens for $t_1/t_2 = 2.7$, with no edge states. Each inset depicts the corresponding positive(green), negative(yellow) and flat(blue) energy bands in the complex plane.

number of boundary modes for this model is $M = 1$ for an H-broken chain and $M = 1$ for an AB-broken chain.

For DCA, the zero-energy eigenmodes for the H-broken chain, $|\Psi_0^{R[L]}\rangle_H$, and for the AB-broken chain, $|\Psi_0^{R[L]}\rangle_{AB}$, will be described through

$$|\Psi_0^{R[L]}\rangle_H = \mathcal{N}_{R[L]}\left(1, 0, 0, r_{R[L]}, 0, 0, \ldots, r_{R[L]}^{N-2}, 0, 0, r_{R[L]}^{N-1}, 0, 0\right) \quad (10a)$$

$$|\Psi_0^{R[L]}\rangle_{AB} = \mathcal{N}_{R[L]}\left(1, 1, 0, \frac{1}{r_{R[L]}}, \frac{1}{r_{R[L]}}, 0, \ldots, \frac{1}{r_{R[L]}^{N-2}}, \frac{1}{r_{R[L]}^{N-2}}, 0, frac1r_{R[L]}^{N-1}, \frac{1}{r_{R[L]}^{N-1}}, 0\right) \quad (10b)$$

where we consider a base of (H_n, A_n, B_n) for the H-broken chain and of (A_n, B_n, H_n) for the AB-broken chain to describe each unit cell n. In Equations (10), $\mathcal{N}_{R[L]}$ are the right or left normalization factors and $r_{L[R]}$ are the left and right localization factors, which are equivalent to those derived for the non-Hermitian SSH model[15]:

$$r_L = -\frac{t_1 + \gamma/2}{t_2} \quad \text{and} \quad r_R = -\frac{t_1 - \gamma/2}{t_2} \quad (11)$$

The presence of destructive interference in the previous eigenmodes of Equations (10) can be clearly visualized through the vanishing amplitudes on A and B sites for the H-broken chain and in H sites for the AB-broken one.

Considering the exponential (de)localization of the eigenmodes into the boundaries, $\langle n|\Psi_0^{R[L]}\rangle = e^{-n/\xi_{R[L]}}$ where $|n\rangle = |e_{A,n}\rangle + |e_{H,n}\rangle + |e_{B,n}\rangle$, the jump on the biorthogonal polarization is constructed through the right and left penetration lengths $\xi_{R[L]}$ of the boundary modes. Knowing that a biorthogonal bulk state forms from right and left states localized at opposite ends $\xi_R = -\xi_L$ and considering that under translational invariance the inverse penetration lengths can be defined through the localization factors as

$$\xi_{R[L]}^{-1}(\mathbf{k}) = \ln|r_{R[L]}(\mathbf{k})| \quad (12)$$

the condition for having a jump between bulk and boundary eigenmodes will be given by $|r_L^* r_R| = 1$.[56] As a result, the biorthogonal polarization acts as an indicator of the topological phase transition using real-space parameters, $\mathcal{P} = f(t_1, t_2, \gamma)$, resulting in a real-space topological invariant.[54]

Despite the fact that the left and right states might be localized at opposite or the same edges, only one of the boundaries will be considered at a time when analyzing the broken lattices reflecting each end of our unbroken chain. This means that the computation of $\mathcal{P}$ with the left and right eigenstates of Equation (10a) will represent the localization of boundary states at $n = 1$ (see purple lines of **Figure 6**) and the computation of $M - \mathcal{P}$ through Equation (10b) will represent the localization of boundary states at $n = N$ (see orange lines of Figure 6) for the original chain (starting with an H site and ending with A and B sites). Considering the shortcut solution used in Ref. [12] for the NH SSH, we obtain the phase transition points of the DCA unbroken chain to be defined as

$$t_1 = \pm\sqrt{t_2^2 + \left(\frac{\gamma}{2}\right)^2} \quad \text{for} \quad |t_2| > \frac{|\gamma|}{2} \quad \text{and} \quad (13a)$$

$$t_1 = \pm\sqrt{-t_2^2 + \left(\frac{\gamma}{2}\right)^2} \quad \text{for} \quad |t_2| < \frac{|\gamma|}{2} \quad (13b)$$

which have been represented in blue lines at Figure 6b and in blue dashed lines at Figure 6a,c. This shows that the appearance of the zero-energy edge states delimited by the biorthogonal polarization is in accordance with the predicted phase transitions from the generalized BZ method used in Ref. [12].

2.2.2. Band Geometry and Topology for DCB

As described before, the wave function associated with the flat band of DCB has a non-trivial dependence on the momentum $\kappa|$ see Appendix A.1. In the following, we will show that this leads to non-trivial quantum metric properties. To begin with, we briefly recall the definition and main properties of the quantum metric $g_{\mu\nu}$ in Hermitian and non-Hermitian systems. In the Hermitian case, the quantum metric[58] is a gauge invariant and measurable quantity[59–61] that can be seen as a momentum-space Riemannian metric.[62–65] It has been shown that $g_{\mu\nu}$ plays a central role in Chern insulators,[66–69] spreading of the Wannier functions,[70] superconducting weight in flat-band superconductors,[71–74] topological semimetals,[75–78] quantum phase transitions[79–81] and in the semiclassical equations for wave-packets.[82] Moreover, the non-Hermitian version of the quantum metric has been originally introduced in Ref. [83] and has been recently shown to be relevant in different kinds of non-Hermitian topological phases[84] (see also Ref. [85] for a more recent work on the subject). In order to define this geometric quantity in the NH case, we first introduce the NH quantum geometric tensor (QGT) $Q_{\mu\nu}^n$, given by

$$Q_{\mu\nu}^n = \frac{1}{2}[\langle\partial_\mu u_n^L|(1 - P_n)|\partial_\nu u_n^R\rangle + \langle\partial_\mu u_n^R|(1 - P_n^\dagger)|\partial_\nu u_n^L\rangle] \quad (14)$$

where n is the band index, $|u_n^{L/R}\rangle$ are the left/right Bloch wave-eigenvectors, $\partial_\mu = \partial_{k_\mu}$ and $P_n = |u_n^R\rangle\langle u_n^L|$ is the projector operator. Thus, the corresponding NH quantum metric tensor is given by the real part of the above tensor, i.e., $g_{\mu\nu} = \mathrm{Re}(Q_{\mu\nu}^n)$ while the imaginary part of the NH QGT corresponds to the NH Berry curvature, namely $F_{\mu\nu}^n = -2\mathrm{Im}(Q_{\mu\nu}^n)$. However, we notice that in 1D systems, the imaginary part of the QGT is absent such that $g_{\mu\nu}$ is the only non-trivial geometric quantity that can be built. For the DCB, the NH quantum metric for the flat and negative energy bands are respectively given by

$$g_{xx}^0(\kappa) = -\frac{t_2^2\gamma^2}{\left(E_-^{DCB}\right)^4} \quad (15)$$

$$g_{xx}^-(\kappa) = -\frac{t_2^2(\gamma^2 - t_1^2 - 2t_2^2 - 4t_1t_2\cos\kappa - t_1^2\cos 2\kappa)}{2\left(E_-^{DCB}\right)^4}$$

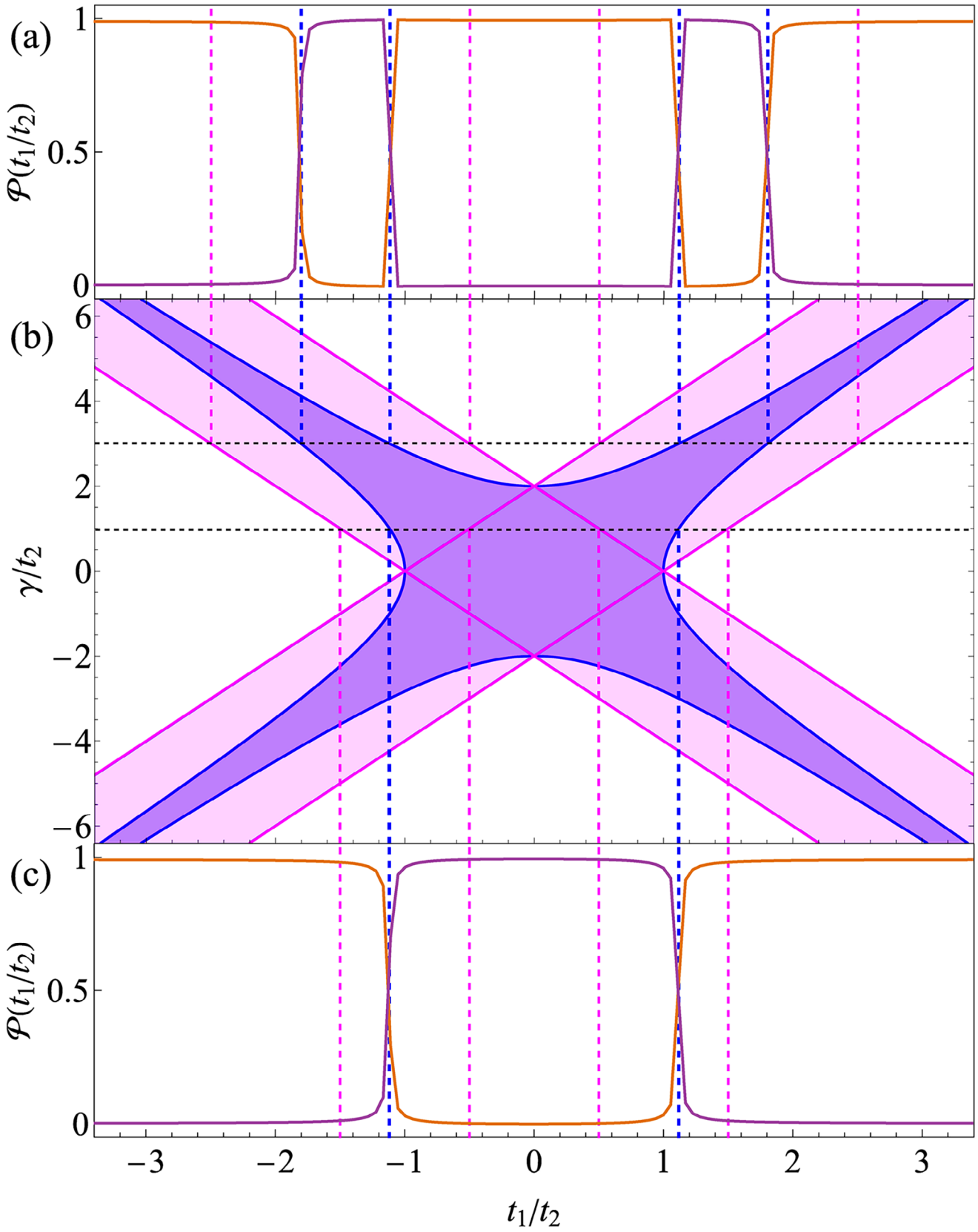

Figure 6. Phase diagram of the DCA model along with the biorthogonal polarization of two cuts in this phase diagram. b) Phase diagram of the non-Hermitian DCA model. In this analysis, pink lines represent the parameter values where exceptional points (EPs) emerge in the eigenenergies under

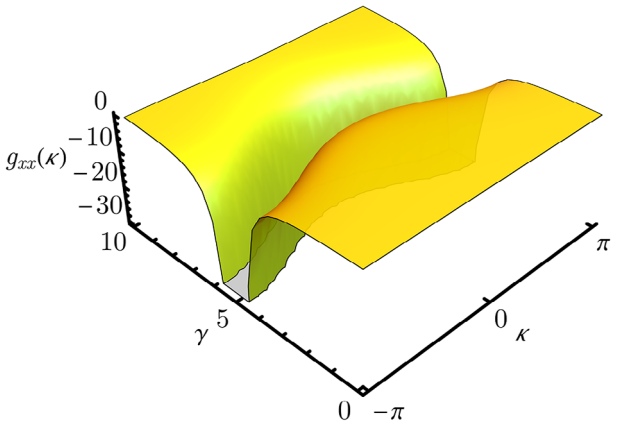

Figure 7. Plot of the quantum metric associated to the flat band (15)of lattice DCB as a function of t_1 and of the non-reciprocal coupling term γ.

We can now make some relevant observations concerning the peculiar band geometry of DCB: first, g^0_{xx} is non-zero only in the NH regime, in which even the flat band acquires some non-trivial geometric features differently from the Hermitian case. In fact, due to its dependence on the energy dispersion, E^{DCB}, the band geometry of the flat band contains information about the exceptional points of DCB. Thus the corresponding quantum metric is divergent at those points, similar to what has been shown in NH models without flat bands.[86,87] Second, another main consequence of the non-trivial behavior of g^0_{xx} is related to the conductivity at the flat band that is robust in the presence of disorder and can even be tremendously boosted, similar to the Hermitian case discussed in Ref. [50]. The boost is obtained for values of γ changing the spectrum from real to imaginary (8)| see **Figure 7**. Third, in the limit $t_1 \to 0$, DCB supports three completely flat bands, and the quantum metric becomes constant for all the bands. This quantum geometry behavior resembles the one related to the Hermitian two-band Creutz ladder, where the quantum metric has been shown to be constant for both flat bands.[88] In this limit, the ratio between g^0_{xx} and g^-_{xx} acquires a simple expression

$$\frac{g^0_{xx}}{g^-_{xx}} = \frac{2\gamma^2}{\gamma^2 - 2t_2^2} \tag{16}$$

which converges to 2 for $\gamma \gg t_2$, i.e., in the strongly NH regime. On the other hand, in the opposite Hermitian limit $\gamma = 0$ and for $t_1 \to 0$, g^-_{xx} is still constant and equal to 1/4 while g^0_{xx} becomes identically null.

To characterize the band topology of DCB, we employ the approach originally proposed in the Hermitian framework in Ref. [89] and then extended in the non-Hermitian systems in Ref. [84], which is based on the construction of suitable momentum-space scalar fields ϕ^{L}_n and ϕ^{R}_n, given by

$$\phi^{\mathrm{L}}_n = -\frac{\mathrm{i}}{2}\log\prod_{\aleph} u^{\mathrm{L}}_{n,\aleph}, \quad \phi^{\mathrm{R}}_n = -\frac{\mathrm{i}}{2}\log\prod_{\aleph} u^{\mathrm{R}}_{n,\aleph} \tag{17}$$

where $u^{\mathrm{L}}_{n,\aleph}$ and $u^{\mathrm{R}}_{n,\aleph}$ denote the non-zero components of $|u^{\mathrm{L}}_n\rangle$ and $|u^{\mathrm{R}}_n\rangle$, respectively. From the above scalar fields in our 1D case, we can define a NH Zak-like phase for the DCB as follows

$$w_n = -\int_0^{2\pi} d\kappa\, \partial_\kappa \phi^{\mathrm{L}}_n = -\int_0^{2\pi} d\kappa\, \partial_\kappa \phi^{\mathrm{R}}_n \tag{18}$$

where the integration is performed in the first Brillouin zone. From this expression, we observe that for the flat band, w_0 is never quantized, which implies a trivial band topology. On the other hand, the lower band carries non-trivial band topology in the following regime

$$w_- = \pi, \quad |t_2| - |t_1| > |\gamma|/2 \tag{19}$$

This result represents a natural but non-trivial generalization of the topological phase supported for $|t_2| > |t_1|$ in the Hermitian model.[34]

2.3. Rotation into a 1D Model with a Flat Band?

In the following, we show how to perform a rotation to a new base choice of the diamond chain, which allows us to have a better understanding of several of the properties we have shown so far. We obtain the new base considering a real or complex linear combination of the site with lower connectivity. The site operators in this new base read

$$\mathcal{A}^\beta_n = \frac{1}{\sqrt{2}}(c_{\mathrm{A},n} + \beta c_{\mathrm{B},n}) \tag{20a}$$

$$\mathcal{H}_n = c_{\mathrm{H},n} \tag{20b}$$

$$\mathcal{B}^\beta_n = \frac{1}{\sqrt{2}}(c_{\mathrm{A},n} - \beta c_{\mathrm{B},n}) \tag{20c}$$

where $\beta = \{1, \mathrm{i}\}$. The matrices U_β associated with this rotation result in:

$$U_\beta = \frac{1}{\sqrt{2}}\begin{pmatrix} 1 & 0 & \beta \\ 0 & \sqrt{2} & 0 \\ 1 & 0 & -\beta \end{pmatrix} \tag{21}$$

periodic boundary conditions (PBC), while blue lines indicate the appearance or disappearance of zero-energy edge states under open boundary conditions (OBC). In the Hermitian system ($\gamma = 0$) under OBC, the phase transition coincides with the one observed in the system under PBC. However, in the non-Hermitian case, the topological phase (purple area) is defined by the OBC system, which broadens the range in which the trivial phase appears (both the pink-shaded and white areas). The dashed lines correspond to the values at which the polarization has been computed analytically for a DCA chain of $N = 100$. In panel (a), the calculation is performed for $\gamma/t_2 = 3$, and in panel (c), it is done at $\gamma/t_2 = 1$, such that when the zero-energy edge states are present (absent), the biorthogonal polarization is $\mathcal{P} = 1(0)$ for the H-broken chain (purple lines) and $\mathcal{P} = 0(1)$ for the AB-broken chain (orange lines). The dashed lines in pink and blue indicate the values of the parameters where EPs occur under PBC and phase transition points arise under OBC, respectively.

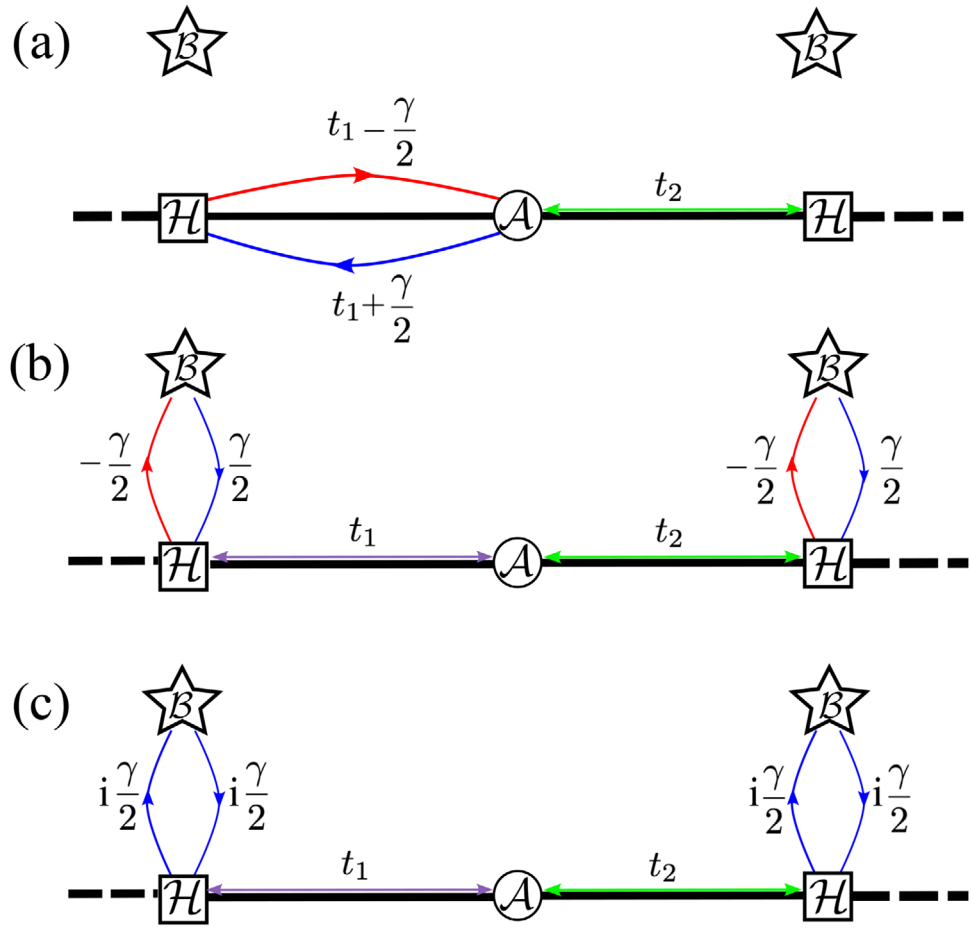

Figure 8. Rotated diamond chain from the DCA to a) a non-Hermitian SSH chain with non-reciprocal hoppings plus disconnected $\mathcal{B}$ sites and from the DCB to a Hermitian SSH chain coupled through b) non-reciprocal hopping parameters to $\mathcal{B}$ sites using U_1 matrix transformation or c) complex hopping parameters to the virtual sites using U_i, respectively.

and applied to the NH Hamiltonian operator in reciprocal space of Equation (2), give rise to the same rotated model of the DCA. The resulting Hamiltonian in reciprocal space reads:

$$h^{\text{Rot}}_{\text{DCA}}(\kappa) = d_x \Sigma^{\text{Rot}}_x + d_y \Sigma^{\text{Rot}}_y \tag{22}$$

being the Σ^{Rot}_x and Σ^{Rot}_y matrices defined as:

$$\Sigma^{\text{Rot}}_x = \begin{pmatrix} 0 & 1 & 0 \\ 1 & 0 & 0 \\ 0 & 0 & 0 \end{pmatrix} \text{ and } \Sigma^{\text{Rot}}_y = \begin{pmatrix} 0 & \text{i} & 0 \\ -\text{i} & 0 & 0 \\ 0 & 0 & 0 \end{pmatrix} \tag{23}$$

which is analogous to the non-Hermitian Stub model of Ref. [48] with $t_3 = 0$. The rotated DCA model, therefore, describes a non-Hermitian SSH chain with non-reciprocal hopping parameters [see **Figure 8**a] formed by $\mathcal{A}$ and H sites decoupled to the $\mathcal{B}$ sites originating the flat band. This rotation helps to understand that in this new base, the NH skin effect and the topological properties should be analogous to the one of the NH SSH model.[15]

The transformation matrices defined in Equation (21) applied to the DCB lattice in reciprocal space described in Equation (7) give rise to two equivalent systems for real and complex β:

$$h^{\text{Rot1}}_{\text{DCB}}(\kappa) = U_1^{-1} h_{\text{DCB}}(\kappa) U_1 = \sqrt{2} \begin{pmatrix} 0 & t_1 + t_2 e^{\text{i}\kappa} & 0 \\ t_1 + t_2 e^{-\text{i}\kappa} & 0 & \frac{\gamma}{2} \\ 0 & -\frac{\gamma}{2} & 0 \end{pmatrix} \tag{24a}$$

$$h^{\text{Rot2}}_{\text{DCB}}(\kappa) = U_{\text{i}}^{-1} h_{\text{DCB}}(\kappa) U_{\text{i}} = \sqrt{2} \begin{pmatrix} 0 & t_1 + t_2 e^{\text{i}\kappa} & 0 \\ t_1 + t_2 e^{-\text{i}\kappa} & 0 & \text{i}\frac{\gamma}{2} \\ 0 & \text{i}\frac{\gamma}{2} & 0 \end{pmatrix} \tag{24b}$$

Both of these models contain a Hermitian SSH chain formed by $\mathcal{A}$ and $\mathcal{H}$ sites that are now coupled to the $\mathcal{B}$ sites in a non-Hermitian fashion, cf. Figures 8b,c. It is important to note that the $\mathcal{B}$ sites are disconnected from each other, thus representing the flat band. However, they are coupled to the Hermitian SSH model. This coupling is found to be non-reciprocal for the first rotation in Equation (24a), where we observe that we have broken

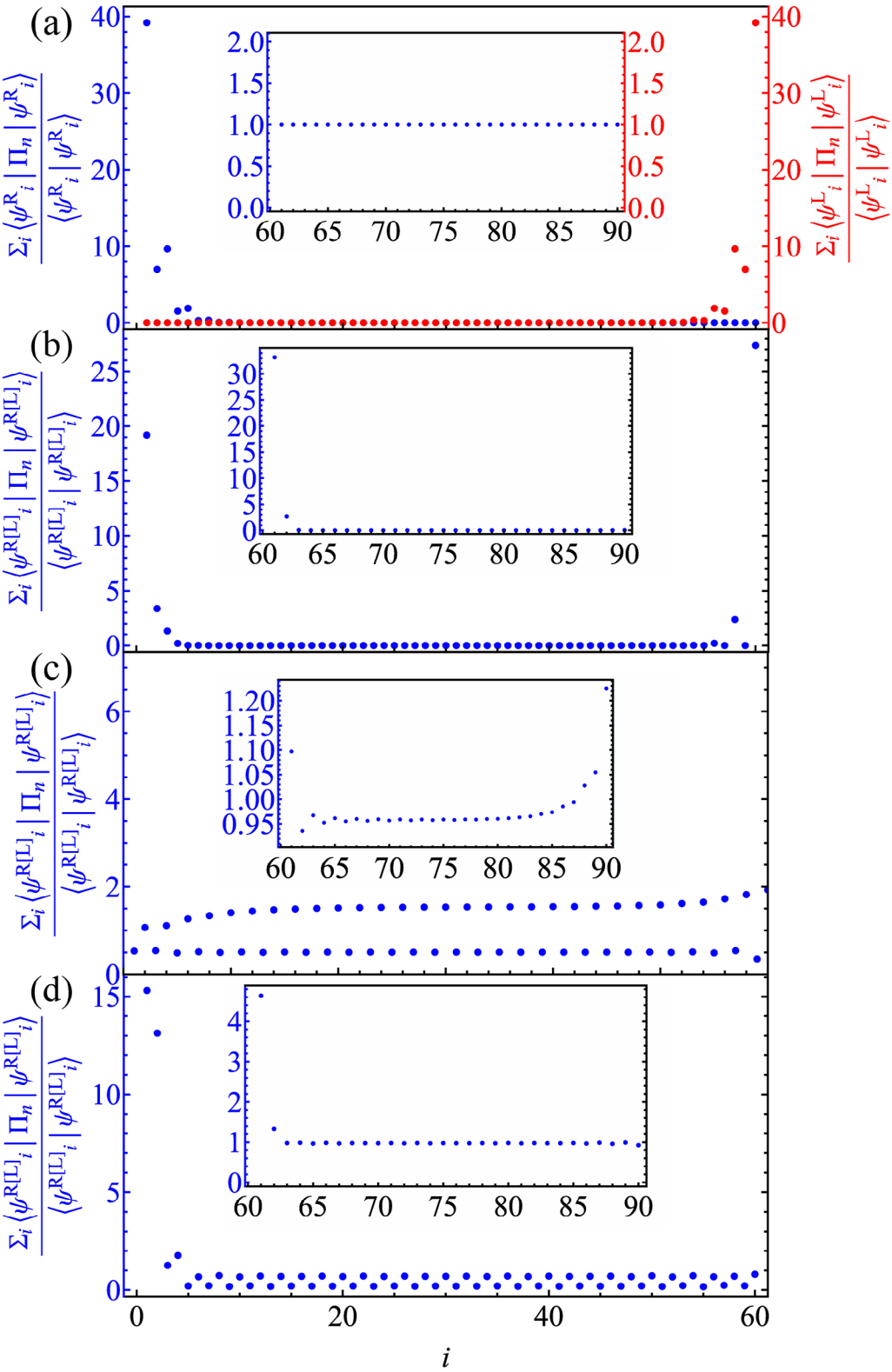

Figure 9. Skin effect for the rotated non-Hermitian DCA and DCB chains represented through the sum of the squared amplitudes of each site i with $N = 30$ and $\gamma = 3$. The upper diagram (a) represents the skin effect of the rotated non-Hermitian DCA system at $t_1/t_2 = 2$, the second panel (b), shows the first case of the rotated non-Hermitian DCB system where the eigenvalues are fully imaginary pairs like at $t_1/t_2 = 0.3$, the third diagram (c) shows the skin effect of the rotated non-Hermitian DCB model skin effect under eigenvalues coming in complex conjugate pairs as in $t_1/t_2 = 1.2$ and the lower one (d) represents the rotated non-Hermitian DCB skin effect for the case in which the spectra is fully real as it happens for $t_1/t_2 = 2.7$. In the present

the inversion symmetry $\mathcal{I} = \Sigma_x|$ see Figure 8b. While the case of the imaginary rotation in Equation (24b), the coupling between the flat band and the Hermitian SSH chain breaks time-reversal symmetry $\mathcal{T} = C|$ see Figure 8c. This rotation helps us to unveil the nature of the NH skin effect we have presented in Figure 5. The dispersive part of the system is a Hermitian SSH model and should not present any skin effect; however, it is connected in a NH fashion to the flat band giving rise to a finite skin effect. It has to be noted that the strength of this skin effect is smaller than in the case of DCA since it originates in the flat band where all the $\mathcal{B}$ sites are disconnected.

In **Figure 9**, we present the results for the skin effect for DCA and DCB, considering the tight-binding representations of Equations (22) and (24). For DCA in Figure 9a, we can clearly observe a skin effect identical to the case of the NH SSH for the $\mathcal{H}$ and $\mathcal{A}$, whereas, for the $\mathcal{B}$ sites corresponding to the flat band, the skin effect is absent. For the case of DCB, we show in Figure 9b–d the results for the same parameter values we used in Figure 5 but in the rotated base, i.e., $\{\mathcal{H}, \mathcal{A}, \mathcal{B}\}$. We clearly observe that now the skin effect that arises in the flat band is transmitted by *proximity* to the Hermitian SSH model via the NH coupling. Most importantly, within this choice of the base, the right, and the left eigenvectors differ only up to a phase factor, for the reason they are identical when representing them in Figure 9b,d.

3. Discussions and Conclusions

In this article, we have investigated the topological properties of a non-Hermitian version of the diamond chain. We have shown that compared to the Hermitian case, there exist two possible non-Hermitian configurations presenting non-trivial topological properties. Specifically, for one of the two configurations that we have named DCA, the system presents properties analogous to a non-Hermitian SSH chain plus a flat band. We have characterized this system by investigating the biorthogonal polarization. The second configuration, which we have named DCB, presents a non-zero quantum metric for the flat band due to the wave function's k dependency. This quantum metric becomes highly divergent near the exceptional points, providing a significant boost when tuning the non-Hermitian parameter γ. The band topology of the DCB configuration indicates that the flat band possesses a trivial nature, while the non-Hermitian Zak phase of the lower band can exhibit a non-trivial band topology. Both systems can be mapped to the SSH model. The DCA system can be transformed into a non-Hermitian SSH model with disconnected sites representing the flat band. In contrast, the DCB model can be similarly transformed into a Hermitian SSH chain, connected in a non-Hermitian fashion to these additional sites representing the flat band. Interestingly, both systems present a NH skin effect. This is especially surprising for DCB, which presents a spectrum in the complex plane that is either real, imaginary, or a combination of both.

Appendix A: Eigenvectors of the Non-Hermitian Diamond Chain

In this appendix, we will present the analytical expressions for the eigenvectors of the two lattice systems, DCA and DCB. We start by introducing the following quantities:

$$\rho_{\pm}(\kappa) = \frac{t_1 \pm \frac{\gamma}{2}}{t_2} + \cos\kappa + \mathrm{i}\sin\kappa = |\rho_{\pm}(\kappa)|e^{\mathrm{i}\phi_{\pm}(\kappa)} \tag{A1}$$

The biorthogonal base for DCA reads:

$$|\psi_{0,\mathrm{R}}\rangle = \frac{1}{\sqrt{2}}(-1, 0, 1) \tag{A2a}$$

$$|\psi_{\alpha,\mathrm{R}}\rangle = \frac{1}{2}\left(1, \frac{E_{\alpha}^{\mathrm{DCA}}}{t_2|\rho_-(\kappa)|e^{\mathrm{i}\phi_-}}, 1\right) \tag{A2b}$$

and

$$|\psi_{0,\mathrm{L}}\rangle = \frac{1}{\sqrt{2}}(-1, 0, 1) \tag{A3a}$$

$$|\psi_{\alpha,\mathrm{L}}\rangle = \frac{1}{2}\left(1, \frac{E_{\alpha}^{\mathrm{DCA}}}{t_2|\rho_+(\kappa)|e^{\mathrm{i}\phi_+}}, 1\right) \tag{A3b}$$

These states fulfill the biorthogonal scalar product[55]:

$$\langle\psi_{\alpha,\beta,\mathrm{R}}|\psi_{\alpha',\beta',\mathrm{L}}\rangle = \delta_{\alpha,\alpha'}\delta_{\beta,\beta'} \tag{A4}$$

whereas the biorthogonal base for DCB reads:

$$|\psi_{0,\mathrm{R}}\rangle = \mathcal{N}\left(-|\rho_+(\kappa)|e^{-\mathrm{i}\phi_+} + \gamma, 0, |\rho_+(\kappa)|e^{\mathrm{i}\phi_+}\right), \tag{A5a}$$

$$|\psi_{\alpha,\mathrm{R}}\rangle = \mathcal{N}\left(\frac{-t_2|\rho_-(\kappa)|e^{-\mathrm{i}\phi_-} + \gamma}{t_2|\rho_+(\kappa)|e^{\mathrm{i}\phi_+}}, \frac{E_{\alpha}^{\mathrm{DCB}}}{t_2|\rho_+(\kappa)|e^{\mathrm{i}\phi_+}}, 1\right) \tag{A5b}$$

and

$$|\psi_{0,\mathrm{L}}\rangle = \mathcal{N}\left(-|\rho_+(\kappa)|e^{-\mathrm{i}\phi_+}|, 0, |\rho_-(\kappa)|e^{\mathrm{i}\phi_-}|\right) \tag{A6a}$$

$$|\psi_{\alpha,\mathrm{L}}\rangle = \mathcal{N}\left(\frac{t_2|\rho_+(\kappa)|e^{\mathrm{i}\phi_+} + \gamma}{t_2|\rho_-(\kappa)|e^{\mathrm{i}\phi_-}}, \frac{E_{\alpha}^{\mathrm{DCB}}}{t_2|\rho_-(\kappa)|e^{\mathrm{i}\phi_-}}, 1\right) \tag{A6b}$$

Here, we have introduced the factor of normalization $\mathcal{N}$ in order to fulfill the biorthogonal scalar product in Equation (A4); the normalization factor is defined as

$$\mathcal{N} = \sqrt{\frac{1}{2} + \frac{2\mathrm{i}\gamma t_2 \sin\kappa}{4\left(t_1^2 + t_2^2\right) - \gamma^2 + 8t_1 t_2\cos\kappa}} \tag{A7}$$

figure, the rotated systems have been represented considering the base ($\mathcal{H}_n$, $\mathcal{A}_n$, $\mathcal{B}_n$). Additionally, the sites of the open chain have been redistributed such that the skin effect of the corresponding $\mathcal{B}$ sites are depicted in the inset of each figure, leaving the main figure for the skin effect originated from the $\mathcal{A}$ and $\mathcal{H}$ sites, respectively.

Table A1. The DCA model is subject to symmetry conditions, each with its specific constraint equation. These equations are fulfilled by applying the symmetry operator on the Hamiltonian, where $\beta = \{1, i\}$.

Symmetry	Equation	Operator
PHS$_t$, $CC^* = 1$	$h(-k) = -Ch^T(k)C^{-1}$	–
PHS$_t$, $CC^* = -1$	$h(-k) = -Ch^T(k)C^{-1}$	–
TRS$_t$, $TT^* = 1$	$h(-k) = Th^T(k)T^{-1}$	–
TRS$_t$, $TT^* = -1$	$h(-k) = Ch^T(k)C^{-1}$	–
PHS$_c$, $CC^* = 1$	$h(-k) = -Ch^*(k)C^{-1}$	$\beta R_{A,B}$, βR_H, $\beta G_{A,B}$, βG_H
PHS$_c$, $CC^* = -1$	$h(-k) = -Ch^*(k)C^{-1}$	–
TRS$_c$, $TT^* = 1$	$h(-k) = Th^*(k)T^{-1}$	$\beta \mathbb{I}_{3\times3}$, $\beta P_{B,A}$
TRS$_c$, $TT^* = -1$	$h(-k) = Th^*(k)T^{-1}$	–
CS, $\Gamma^2 = 1$	$h(k) = -\Gamma h^\dagger(k)\Gamma^{-1}$	–
Pseudo-Hermiticity, $\eta^2 = 1$	$h(k) = \eta h^\dagger(k)\eta^{-1}$	–
SLS, $S^2 = 1$	$h(k) = -Sh(k)S^{-1}$	$R_{A,B}$, R_H, $G_{A,B}$, G_H
Parity, $P^2 = 1$	$h(-k) = Ph(k)P^{-1}$	–
Parity-time, $(PT)(PT)^* = 1$	$h(k) = (PT)h^*(k)(PT)^{-1}$	–
Parity-time, $(PT)(PT)^* = -1$	$h(k) = (PT)h^*(k)(PT)^{-1}$	–

Table A2. The DCB model is subject to symmetry conditions, each with its specific constraint equation. These equations are fulfilled by applying the symmetry operator on the Hamiltonian, where $\beta = \{1, i\}$.

Symmetry	Equation	Operator
PHS$_t$, $CC^* = 1$	$h(-k) = -Ch^T(k)C^{-1}$	–
PHS$_t$, $CC^* = -1$	$h(-k) = -Ch^T(k)C^{-1}$	$\beta G_{A,B}$, βG_H
TRS$_t$, $TT^* = 1$	$h(-k) = Th^T(k)T^{-1}$	$\beta P_{B,A}$
TRS$_t$, $TT^* = -1$	$h(-k) = Ch^T(k)C^{-1}$	–
PHS$_c$, $CC^* = 1$	$h(-k) = -Ch^*(k)C^{-1}$	$\beta R_{A,B}$, βR_H
PHS$_c$, $CC^* = -1$	$h(-k) = -Ch^*(k)C^{-1}$	–
TRS$_c$, $TT^* = 1$	$h(-k) = Th^*(k)T^{-1}$	$\beta \mathbb{I}_{3\times3}$
TRS$_c$, $TT^* = -1$	$h(-k) = Th^*(k)T^{-1}$	–
CS, $\Gamma^2 = 1$	$h(k) = -\Gamma h^\dagger(k)\Gamma^{-1}$	$G_{A,B}$, G_H
Pseudo-Hermiticity, $\eta^2 = 1$	$h(k) = \eta h^\dagger(k)\eta^{-1}$	$P_{B,A}$
SLS, $S^2 = 1$	$h(k) = -Sh(k)S^{-1}$	$R_{A,B}$, R_H
Parity, $P^2 = 1$	$h(-k) = Ph(k)P^{-1}$	–
Parity-time, $(PT)(PT)^* = 1$	$h(k) = (PT)h^*(k)(PT)^{-1}$	–
Parity-time, $(PT)(PT)^* = -1$	$h(k) = (PT)h^*(k)(PT)^{-1}$	–

A.2. Table of Symmetries

In this appendix, we present the table on the symmetries of DBA and DCB (Tables A1 and A2). We introduce the following auxiliary matrices:

$$R_H = \begin{pmatrix} -1 & 0 & 0 \\ 0 & 1 & 0 \\ 0 & 0 & -1 \end{pmatrix} \tag{A8a}$$

$$R_{A,B} = \begin{pmatrix} 1 & 0 & 0 \\ 0 & -1 & 0 \\ 0 & 0 & 1 \end{pmatrix} \tag{A8b}$$

$$P_{B,A} = \begin{pmatrix} 0 & 0 & 1 \\ 0 & 1 & 0 \\ 1 & 0 & 0 \end{pmatrix} \tag{A8c}$$

$$G_H = R_H P_{B,A}, \quad \text{and} \tag{A8d}$$

$$G_{A,B} = R_{A,B} P_{B,A}, \tag{A8e}$$

which represent different symmetry operations. Let's consider the following matrices representing a simplified version of the Hamiltonians of the DCA and DCB models in reciprocal space:

$$h_{DC} = \begin{pmatrix} 0 & t_{A\to H} & 0 \\ t_{H\to A} & 0 & t_{H\to B} \\ 0 & t_{B\to H} & 0 \end{pmatrix} \tag{A9}$$

being h_{DCB} like h_{DCA} but changing $t \to t'$. The matrix R_H when applied at the left of the Hamiltonians described in Equation (A10) changes the sign of the H-outgoing hoppings, $t^{(\prime)}_{H\to A,B} \Rightarrow -t^{(\prime)}_{H\to A,B}$. Similarly, the matrix $R_{A,B}$, when applied at the left of the Hamiltonians, changes the sign of the A– and B–outgoing hoppings, $t^{(\prime)}_{A,B\to H} \Rightarrow -t^{(\prime)}_{A,B\to H}$. Consequently, when the full transformations are applied, the resulting matrix is a complete sign flip for both transformations: $h \Rightarrow R_H h R_H^{-1} = -h$ and $h \Rightarrow R_{A,B} h R_{A,B}^{-1} = -h$.

The permutation matrix $P_{B,A}$ exchanges the hopping parameters between the A and B sites $t^{(\prime)}_{H\to A,B} \Rightarrow t^{(\prime)}_{H\to B,A}$ and $t^{(\prime)}_{A,B\to H} \Rightarrow t^{(\prime)}_{B,A\to H}$. Consequently, the transformation matrices G_H and $G_{A,B}$ combine both transformations, resulting in an overall sign flip and a permutation between the A and B sites:

$$G h_{DC} G^{-1} = \begin{pmatrix} 0 & -t_{B\to H} & 0 \\ -t_{H\to B} & 0 & -t_{H\to A} \\ 0 & -t_{A\to H} & 0 \end{pmatrix} \tag{A10}$$

Acknowledgements

The authors acknowledged useful discussions with Duy Hoang Minh Nguyen and Alejandro Sebastián Gómez Gómez. C.M.S, M.A.J.H, and D.B. acknowledged the support from the Spanish MICINN-AEI through Project No. PID2020-120614GB-I00 (ENACT). D.B. further acknowledged the support from Transnational Common Laboratory *Quantum – ChemPhys* and the Department of Education of the Basque Government through the project PIBA_2023_1_0007. A.G.E., D.B., M.A.J.H., and C.M.S. acknowledged funding from the IKUR Strategy under the collaboration agreement between Ikerbasque Foundation and DIPC on behalf of the Department of Education of the Basque Government, Programa de ayudas de apoyo a los agentes de la Red Vasca de Ciencia, Tecnología e Innovación acreditados en la categoría de Centros de Investigación Básica y de Excelencia (Programa BERC) from the Departamento de Universidades e Investigación del Gobierno Vasco and Centros Severo Ochoa AEI/CEX2018-000867-S from the Spanish Ministerio de Ciencia e Innovación and the

Gipuzkoa Provincial Council within the QUAN-000021-01 project. A.G.E., M.A.J.H., and C.M.S. acknowledged support from the Spanish Ministerio de Ciencia e Innovación (PID2022-142008NB-I00) and the Basque Government Elkartek program (KK-2023/00016). F.K.K. acknowledges funding from the European Union via the ERC Starting Grant "NTopQuant". Views and opinions expressed are, however, those of the authors only and do not necessarily reflect those of the European Union or the European Research Council (ERC). Neither the European Union nor the ERC can be held responsible for them.

Conflict of Interest

The authors declare no conflict of interest.

Data Availability Statement

The data that support the findings of this study are available from the corresponding author upon reasonable request.

Keywords

non-Hermitian, skin effect, topology

Received: July 17, 2023
Revised: September 26, 2023
Published online:

[1] E. J. Bergholtz, J. C. Budich, F. K. Kunst, *Rev. Mod. Phys.* **2021**, *93*, 015005.
[2] Y. Ashida, Z. Gong, M. Ueda, *Adv. Phys.* **2020**, *69*, 249.
[3] L. Ding, Z. Lin, S. Ke, B. Wang, P. Lu, *Opt. Express* **2021**, *29*, 24373.
[4] N. Okuma, M. Sato, *Annu. Rev. Condens. Matter Phys.* **2022**, *14*, 83.
[5] Q. Wang, Y. D. Chong, *J. Opt. Soc. Am. B* **2023**, *40*, 1443.
[6] A. Ghatak, M. Brandenbourger, J. van Wezel, C. Coulais, *Proc. Natl. Acad. Sci. U.S.A.* **2020**, *117*, 29561.
[7] C. M. Bender, S. Boettcher, *Phys. Rev. Lett.* **1998**, *80*, 5243.
[8] C. M. Bender, *Rep. Progr. Phys.* **2007**, *70*, 947.
[9] A. Mostafazadeh, *J. Math. Phys.* **2002**, *43*, 205.
[10] K. Kawabata, K. Shiozaki, M. Ueda, M. Sato, *Phys. Rev. X* **2019**, *9*, 041015.
[11] C.-K. Chiu, J. C. Y. Teo, A. P. Schnyder, S. Ryu, *Rev. Mod. Phys.* **2016**, *88*, 035005.
[12] S. Yao, Z. Wang, *Phys. Rev. Lett.* **2018**, *121*, 086803.
[13] X. Zhang, T. Zhang, M.-H. Lu, Y.-F. Chen, *Adv. Phys.: X* **2022**, *7*, 2109431.
[14] R. Lin, T. Tai, L. Li, C. H. Lee, *Front. Phys.* **2023**, *18*, 53605.
[15] F. K. Kunst, E. Edvardsson, J. C. Budich, E. J. Bergholtz, *Phys. Rev. Lett.* **2018**, *121*, 026808.
[16] S. Yao, F. Song, Z. Wang, *Phys. Rev. Lett.* **2018**, *121*, 136802.
[17] K. Yokomizo, S. Murakami, *Phys. Rev. Lett.* **2019**, *123*, 066404.
[18] N. Hatano, D. R. Nelson, *Phys. Rev. Lett.* **1996**, *77*, 570.
[19] T. E. Lee, *Phys. Rev. Lett.* **2016**, *116*, 133903.
[20] S. Lieu, *Phys. Rev. B* **2018**, *97*, 045106.
[21] E. Edvardsson, F. K. Kunst, T. Yoshida, E. J. Bergholtz, *Phys. Rev. Res.* **2020**, *2*, 043046.
[22] Z. Gong, Y. Ashida, K. Kawabata, K. Takasan, S. Higashikawa, M. Ueda, *Phys. Rev. X* **2018**, *8*, 031079.
[23] H. Shen, B. Zhen, L. Fu, *Phys. Rev. Lett.* **2018**, *120*, 146402.
[24] D. S. Borgnia, A. J. Kruchkov, R.-J. Slager, *Phys. Rev. Lett.* **2020**, *124*, 056802.
[25] N. Okuma, K. Kawabata, K. Shiozaki, M. Sato, *Phys. Rev. Lett.* **2020**, *124*, 086801.
[26] K. Zhang, Z. Yang, C. Fang, *Phys. Rev. Lett.* **2020**, *125*, 126402.
[27] W. Su, J. Schrieffer, A. J. Heeger, *Phys. Rev. Lett.* **1979**, *42*, 1698.
[28] W.-P. Su, J. Schrieffer, A. Heeger, *Phys. Rev. B* **1980**, *22*, 2099.
[29] A. J. Heeger, S. Kivelson, J. Schrieffer, W.-P. Su, *Rev. Mod. Phys.* **1988**, *60*, 781.
[30] D. Halder, S. Ganguly, S. Basu, *J. Phys.: Condens. Matter* **2022**, *35*, 105901.
[31] J. Vidal, B. Douçot, R. Mosseri, P. Butaud, *Phys. Rev. Lett.* **2000**, *85*, 3906.
[32] D. Bercioux, M. Governale, V. Cataudella, V. M. Ramaglia, *Phys. Rev. Lett.* **2004**, *93*, 056802.
[33] D. Bercioux, M. Governale, V. Cataudella, V. M. Ramaglia, *Phys. Rev. B* **2005**, *72*, 075305.
[34] D. Bercioux, O. Dutta, E. Rico, *Ann. Phys. (Berl.)* **2017**, *529*, 1600262.
[35] M. Rizzi, V. Cataudella, R. Fazio, *Phys. Rev. B* **2006**, *73*, 100502.
[36] C. Cartwright, G. De Chiara, M. Rizzi, *Phys. Rev. B* **2018**, *98*, 184508.
[37] M. Hyrkäs, V. Apaja, M. Manninen, *Phys. Rev. A* **2013**, *87*, 023614.
[38] S. Mukherjee, M. Di Liberto, P. Öhberg, R. R. Thomson, N. Goldman, *Phys. Rev. Lett.* **2018**, *121*, 075502.
[39] M. N. Huda, S. Kezilebieke, P. Liljeroth, *Phys. Rev. Res.* **2020**, *2*, 043426.
[40] D. Leykam, S. Flach, Y. D. Chong, *Phys. Rev. B* **2017**, *96*, 064305.
[41] S. Ke, D. Zhao, J. Fu, Q. Liao, B. Wang, P. Lu, *IEEE J. Sel. Top. Quantum Electron.* **2019**, *26*, 1.
[42] S. M. Zhang, L. Jin, *Phys. Rev. Res.* **2020**, *2*, 033127.
[43] J. R. Parkavi, V. K. Chandrasekar, M. Lakshmanan, *Phys. Rev. A* **2021**, *103*, 023721.
[44] J. R. Parkavi, V. Chandrasekar, *Optik* **2022**, *271*, 170129.
[45] S. Zhang, L. Jin, Z. Song, *Chin. Phys. B* **2022**, *31*, 010312.
[46] I. Amelio, N. Goldman, *Lasing, quantum geometry and coherence in non-Hermitian flat bands*, **2023**, arXiv:2308.08418.
[47] C. Shu-Yue, J. Chuang, K. Shao-Lin, W. Bing, L. Pei-Xiang, *Acta Phys. Sin.* **2022**, *71*, 174201.
[48] J. Bartlett, H. Hu, E. Zhao, *Phys. Rev. B* **2021**, *104*, 195131.
[49] X. Xu, H. Liu, Z. Zhang, Z. Liang, *J. Condens. Matter Phys.* **2020**, *32*, 425402.
[50] G. Bouzerar, *Phys. Rev. B* **2022**, *106*, 125125. 2205.06164.
[51] R. Koch, J. C. Budich, *Eur. Phys. J. D* **2020**, *74*, 1.
[52] V. M. Alvarez, J. B. Vargas, L. F. Torres, *Phys. Rev. B* **2018**, *97*, 121401.
[53] K. Zhang, Z. Yang, C. Fang, *Nat. Commun.* **2022**, *13*, 2496.
[54] E. Edvardsson, F. K. Kunst, E. J. Bergholtz, *Phys. Rev. B* **2019**, *99*, 081302.
[55] D. C. Brody, *J. Phys. A: Math. Theor.* **2013**, *47*, 035305.
[56] F. K. Kunst, *Solvable Topological Boundaries*, Ph.D. thesis, school Stockholm University, Department of Physics **2019**.
[57] F. K. Kunst, G. van Miert, E. J. Bergholtz, *Phys. Rev. B* **2019**, *99*, 085426.
[58] J. P. Provost, G. Vallee, *Commun. Math. Phys.* **1980**, *76*, 289.
[59] T. Ozawa, N. Goldman, *Phys. Rev. B* **2018**, *97*, 201117.
[60] M. Chen, null, C. Li, G. Palumbo, Y.-Q. Zhu, N. Goldman, P. Cappellaro, *Science* **2022**, *375*, 1017.
[61] X. Tan, D.-W. Zhang, Z. Yang, J. Chu, Y.-Q. Zhu, D. Li, X. Yang, S. Song, Z. Han, Z. Li, Y. Dong, H.-F. Yu, H. Yan, S.-L. Zhu, Y. Yu, *Phys. Rev. Lett.* **2019**, *122*, 210401.
[62] R. Resta, *Eur. Phys. J. B* **2011**, *79*, 121.
[63] G. Palumbo, *Eur. Phys. J. Plus* **2018**, *133*, 23.
[64] G. von Gersdorff, W. Chen, *Phys. Rev. B* **2021**, *104*, 195133.
[65] D. Liska, V. Gritsev, *SciPost Phys.* **2021**, *10*, 020.
[66] R. Roy, *Phys. Rev. B* **2014**, *90*, 165139.
[67] C. H. Lee, M. Claassen, R. Thomale, *Phys. Rev. B* **2017**, *96*, 165150.
[68] T. Ozawa, B. Mera, *Phys. Rev. B* **2021**, *104*, 045103.
[69] C. Northe, G. Palumbo, J. Sturm, C. Tutschku, E. M. Hankiewicz, *Phys. Rev. B* **2022**, *105*, 155410.
[70] N. Marzari, D. Vanderbilt, *Phys. Rev. B* **1997**, *56*, 12847.
[71] S. Peotta, P. Törmä, *Nat. Comm.* **2015**, *6*, 8944.
[72] P. Törmä, S. Peotta, B. A. Bernevig, *Nat. Rev. Phys.* **2022**, *4*, 528.

[73] M. Thumin, G. Bouzerar, *Phys. Rev. B* **2023**, *107*, 214508.
[74] P. He, H.-T. Ding, S.-L. Zhu, *Phys. Rev. A* **2021**, *103*, 043329.
[75] G. Palumbo, N. Goldman, *Phys. Rev. Lett.* **2018**, *121*, 170401.
[76] G. Salerno, N. Goldman, G. Palumbo, *Phys. Rev. Res.* **2020**, *2*, 013224.
[77] Y.-P. Lin, W.-H. Hsiao, *Phys. Rev. B* **2021**, *103*, L081103.
[78] Y. Hwang, J. Jung, J.-W. Rhim, B.-J. Yang, *Phys. Rev. B* **2021**, *103*, L241102.
[79] B. Mera, C. Vlachou, N. Paunković, V. R. Vieira, O. Viyuela, *Phys. Rev. B* **2018**, *97*, 094110.
[80] A. Marrazzo, R. Resta, *Phys. Rev. Lett.* **2019**, *122*, 166602.
[81] M. S. M. de Sousa, A. L. Cruz, W. Chen, *Phys. Rev. B* **2023**, *107*, 205133.
[82] M. F. Lapa, T. L. Hughes, *Phys. Rev. B* **2019**, *99*, 121111.
[83] D.-J. Zhang, Q.-h. Wang, J. Gong, *Phys. Rev. A* **2019**, *99*, 042104.
[84] Y.-Q. Zhu, W. Zheng, S.-L. Zhu, G. Palumbo, *Phys. Rev. B* **2021**, *104*, 205103.
[85] C. C. Ye, W. L. Vleeshouwers, S. Heatley, V. Gritsev, C. M. Smith, *Quantum Geometry of Non-Hermitian Topological Systems*, **2023**, arXiv:2305.17675.
[86] D. D. Solnyshkov, C. Leblanc, L. Bessonart, A. Nalitov, J. Ren, Q. Liao, F. Li, G. Malpuech, *Phys. Rev. B* **2021**, *103*, 125302.
[87] Q. Liao, C. Leblanc, J. Ren, F. Li, Y. Li, D. Solnyshkov, G. Malpuech, J. Yao, H. Fu, *Phys. Rev. Lett.* **2021**, *127*, 107402.
[88] L. Liang, S. Peotta, A. Harju, P. Törmä, *Phys. Rev. B* **2017**, *96*, 064511.
[89] G. Palumbo, N. Goldman, *Phys. Rev. B* **2019**, *99*, 045154.